Applied Physics Research; Vol. 7, No. 5; 2015
ISSN 1916-9639 E-ISSN 1916-9647
Published by Canadian Center of Science and Education

# Fabrication of Gas Sensor Device for $H_2$ and $NO_2$ from Porous Silicon

Waleed Bdaiwi[1]

[1] Department of Physics, College of Education for Pure Science, University Anbar, Iraq

Correspondence: Waleed Bdaiwi, Department of Physics, College of Education for Pure Science, University Anbar, Iraq. Email: wdbedeawy@yahoo.com

Received: June 26, 2014 Accepted: July 23, 2015 Online Published: August 12, 2015

doi:10.5539/apr.v7n5p1 URL: http://dx.doi.org/10.5539/apr.v7n5p1

**Abstract**

A nanocrystalline porous silicon (PS) layer was prepared by electrochemical etching method of p–type silicon wafer in hydrofluoric acid (HF). The properties of porous silicon structure under various etching times (10–50 min), HF concentrations, and current density were studied. The study included photoluminescence (PL), morphology, x–ray, and gas sensor. The results (PL) spectra (peak wavelength) can be shifted from (505 to 625) nm. PL analysis indicated that the energy band gap can be tuned from (1.984–2.455) eV with respect to etched time. Atomic Force Microscopy (AFM) analysis showed that the PS layer had a sponge–like structure. Surface roughness and the pyramid–like hillocks on the entire surface play an important role in variation visible luminescence. The AFM images shows that the average diameter of the PS layer pore and thickness the Silicon decreased when etching time increase and the average diameter particleboard ranged from (80.8–35.4) nm. PS X–ray topography studies that the skeleton maintained its silicon crystalline structure after anodization. PS Sensors were fabricated and tested successfully on $H_2$ and $No_2$ gas.

**Keywords:** porous silicon, gas sensor, photoluminescence, x–ray, AFM

## 1. Introduction

Porous silicon (PS) is widely used in a variety of fields because of its low cost, large surface area within a small volume, and ability to modulate its refractive index as a function of depth PS. A PS consists of a network of nanoscale–sized silicon wires and voids that form when crystalline silicon wafers are etched electrochemically in hydrofluoric–acid (HF)–based electrolyte solution under anodization conditions (Nayef & Muayad, 2013; Šalucha & Marcinkevičius, 2007). PS structures have good mechanical robustness, chemical stability, and compatibility with existing silicon technology. Thus, it has a wide range of potential applications, including bio sensors, photovoltaic devices, gas sensors, humidity sensors, vapor sensors, and pressure sensors (Dubey & Gautam, 2009; Dubey, Patil, Bange, & Gautam, 2007; Agarwal & Del Rıo, 2003; Oton et al., 2003; Setzu, Ferrand, & Romestain, 2000; Salcedo, Ramirez Fernandez, & Galeazzo, 1997). PS can also be used for anode materials of Li rechargeable batteries because of its larger surface (Mizsei, 2007; Jalkanen, Tuura, Mäkilä, & Salonen, 2010). Fabrication of PS micro cavity as optical sensor device (Mishra, Patel, & Vohra, 2014).

Silicon crystallites have diameters varying from units of nanometers to tens of micrometers depending on the formation parameters, such as current density, electrolyte concentration, etching time, and substrate type (Galeazzo, Peres, Santos, Peixoto & Ramirez-Fernandez, 2003). The ability to control porosity makes PS suitable for gas sensing application (Watanabe, Okada, Choe, & Sato, 1996; Skryshevsky, 2000; Lee, Jeon, Lee, & Choi, 2003). The sensitivity of these devices depends on the size of the point contact. In general, a higher sensitivity is achieved in detectors with lower contact dimensions. A porous structure and a large internal surface imply high sensitivity to physical and chemical properties, thereby making PS a promising material for commercial sensors (Bratkowski, Korcala, Łukasiak, Borowski, & Bała, 2005; Dian, Konečný, Broncová, Kronďák, & Matolínová, 2013; Saplagio et al., 2014). PS properties, such as photoluminescence (PL) and electrical conductivity, change when molecules are adsorbed to its surface (Galeazzo, Peres, Santos, Peixoto, & Ramirez-Fernandez, 2003; Möller, Chorin, & Koch, 1995). PL is critically dependent on various processing conditions (Marotti, Quagliata, & Dalchiele, 2003; Mizuno, Koyama, & Koshida, 1996) with or without illumination, as well as on the properties of the silicon substrate, such as doping level and crystal orientation (Marotti, Quagliata, & Dalchiele, 2003; Mizuno, Koyama, & Koshida, 1996). Physical Features of PS are connected with quantum confinement effects, i. e., with a change of the band diagram and increase of effective band gap (Timokhov & Timokhov, 2004; Nayef, 2013). The PS energy band gap has been determined through the peak of the PL spectra (Lehmann, &

Gösele, 1991). X–ray diffraction (XRD) measurements presented a feature related to crystalline materials. Each diffraction peak consisted of a sharp peak and a broad diffraction around the peak (Lehmann, & Gösele, 1991).

A previous study found that the fraction of atoms at the grain boundary increased when the crystal size decreased in the gas sensor. As a result, grain boundaries contained high density of defects, including vacancies and dangling bonds, which plays an important role in the transport properties of materials electrons. The sensitivity of the nanocrystalline sensors has been shown to be proportional to 1/D, where D is the average grain size. Nanocrystalline structures can also reduce the sensor operating temperature (Lehmann, & Gösele, 1991).

## 2. Experimental Method

### *2.1 Device Fabrication*

Devices were fabricated in silicon substrate orientation material using a p–type crystalline silicon wafer with <111> orientation. The PS layer was prepared by using the electrochemical etching technique in the electrolyte solution of ($HF:H_2O:C_2H_5OH$ ) with a volume fraction of (1:1:2). The mixing of ethanol in the electrolyte solution aided in improving the lateral homogeneity and uniformity of the porous silicon layer by promoting hydrogen bubble removal (Rothschild & Komem, 2004). The simplest cell used to anodize silicon is shown in Figure (1). The anode was composed of silicon wafer, while the cathode was composed of platinum or any HF–resistant and conducting material. The cell body was composed of a highly acid–resistant polymer, such as Teflon. Silicon wafer surfaces that served as anodes in contact with HF solution, including the cleaved edges. The advantage of this equipment is its simplicity (Doğan et al., 2013). PS samples (p–type) were prepared at a constant current density of 20 $mA/cm^2$ under different times (10–50 min). In addition, pure gold (99.999) was deposited on the PS surface to obtain high conductivity (Figure 2).

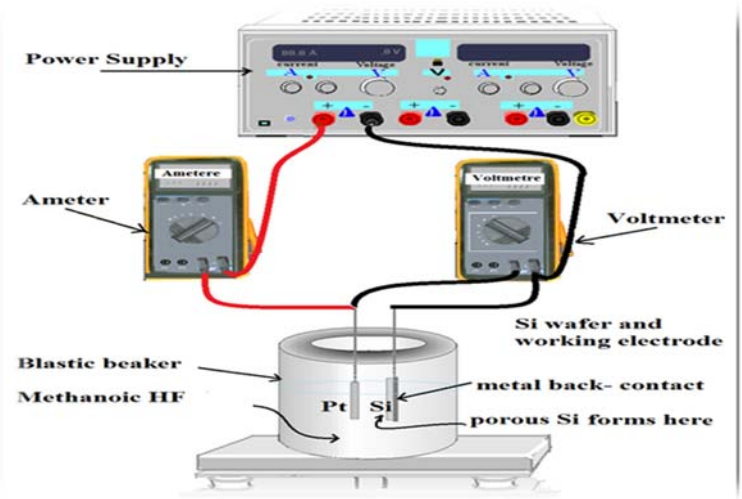


Figure 1. Schematic system of the electrochemical etching

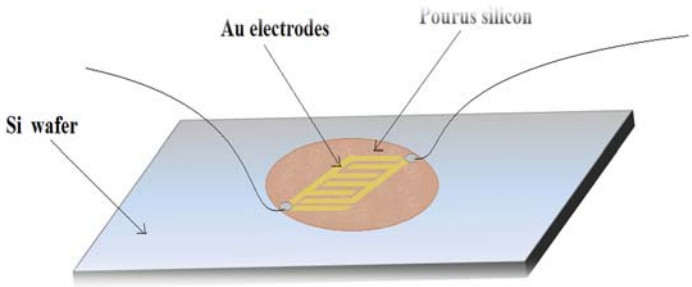


Figure 2a. Schematic of the Shape of the Electrode

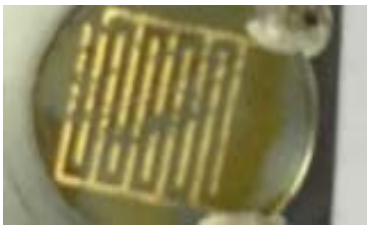

Figure 2b. Schematic of the Shape of the Gold Electrode

### *2.2 Gas Exposure and Measurements*

PL was measured by using a monochromator at a wavelength range of 400–900 nm. The surface morphology and roughness of the prepared samples were obtained using atomic force microscopy (AFM). AFM is useful for obtaining two− and three – dimension topographic information. X–Ray diffraction (XRD) utilizes the morphological properties of the PS layer, such as nanocrystalline size, the structure aspect of the PS layer, and lattice constant. Devices were tested in saturated ambient $No_2$ and $H_2$ gas.

## 3. Results and Discussion

### *3.1 Optical Properties*

Figure 3 shows the photoluminescence at room temperature of samples PS1, PS2, PS3, PS4, and PS5 by adjusting the anodization current density to 30mA/cm$^2$ variations and etching time to 10, 20, 30, 40, and 50 min. Table 1 shows that the peak of the red band emission ranged from 542–629 nm in the PL spectra of PS. However, the band gap can be tuned to 1.984–2.455 eV at various etching time. An increase in etching time resulted in an increase in the diameter of the pores. The shifting of the red emission can be observed in figure crystallites based on the variations of anodization parameters. Red emission decreased as wafer resistivity increased as shown in the nanostructure section, whereas the optical band gap appeared to increase. These results are similar to the relationship between the optical band gap and the Si nanocrystallites.

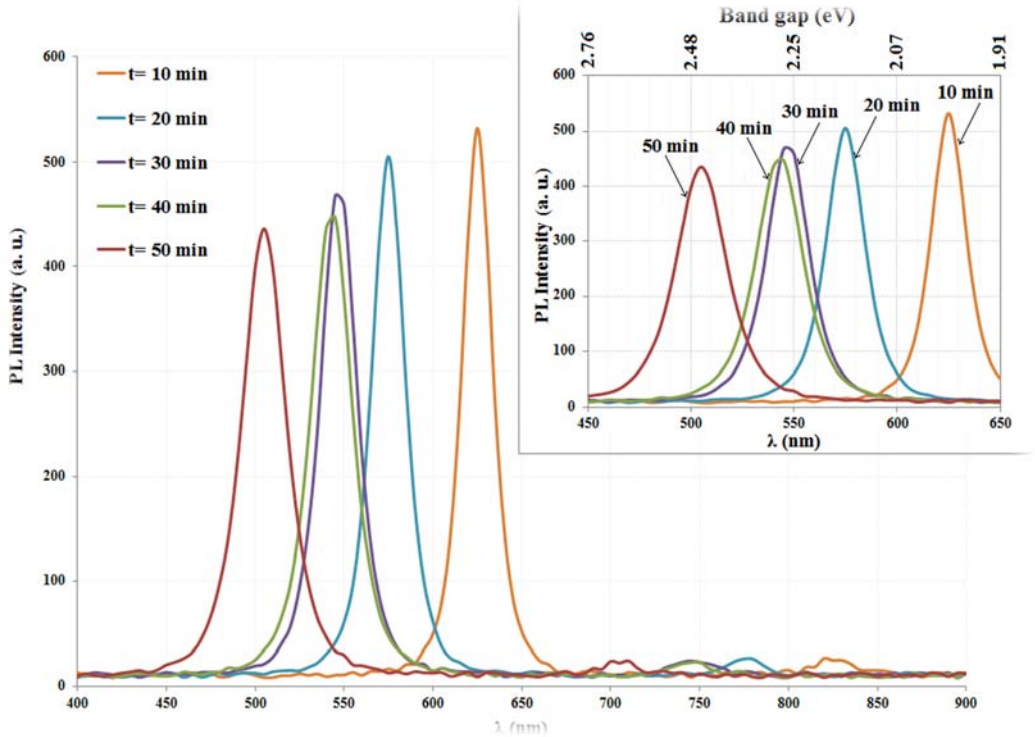


Figure 3. Schematic PL spectra of the porous silicon with various etching times.

Table 1. Variations in Wavelength and Energy gap with various etching time

| time (min) | $\lambda_{max}$ (nm) | $E_g$ (eV) |
|---|---|---|
| 10 | 625 | 1.984 |
| 20 | 575 | 2.157 |
| 30 | 547 | 2.267 |
| 40 | 543 | 2.284 |
| 50 | 505 | 2.455 |

*3.2 Morphological Properties*

**etching time 10 min**

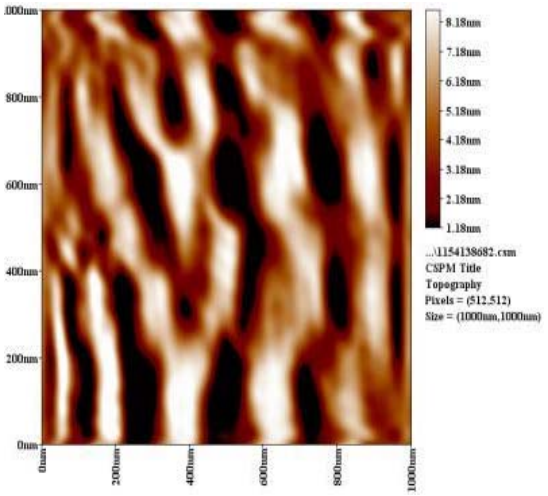


**etching time 10 min**

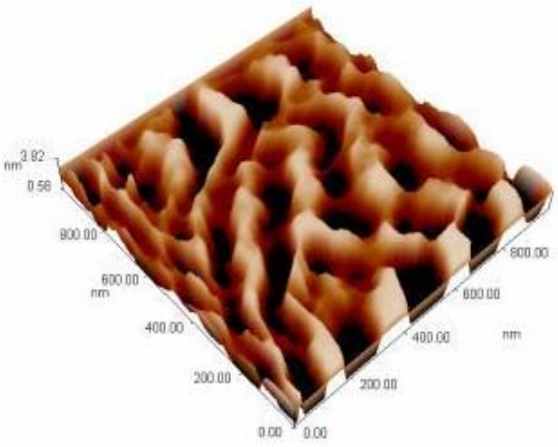


**etching time 20 min**

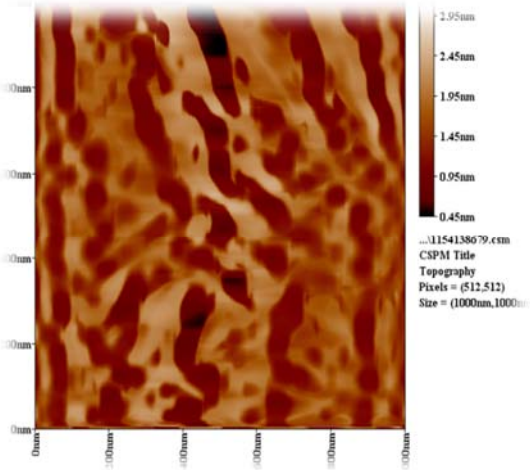


**etching time 20 min**

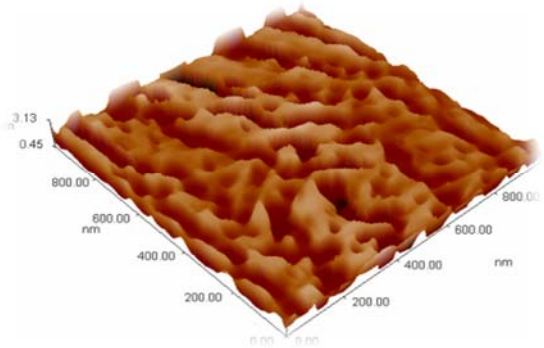


**etching time 30 min**

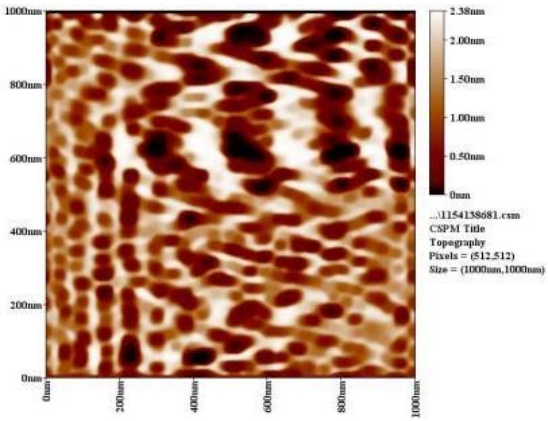


**etching time 30 min**

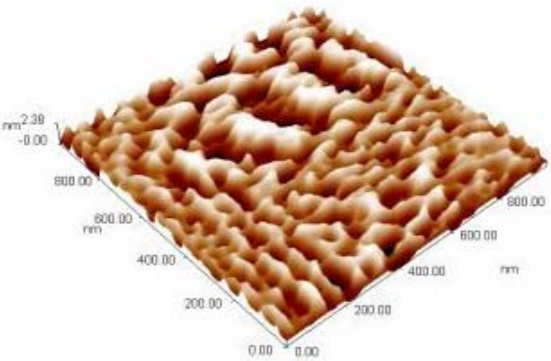

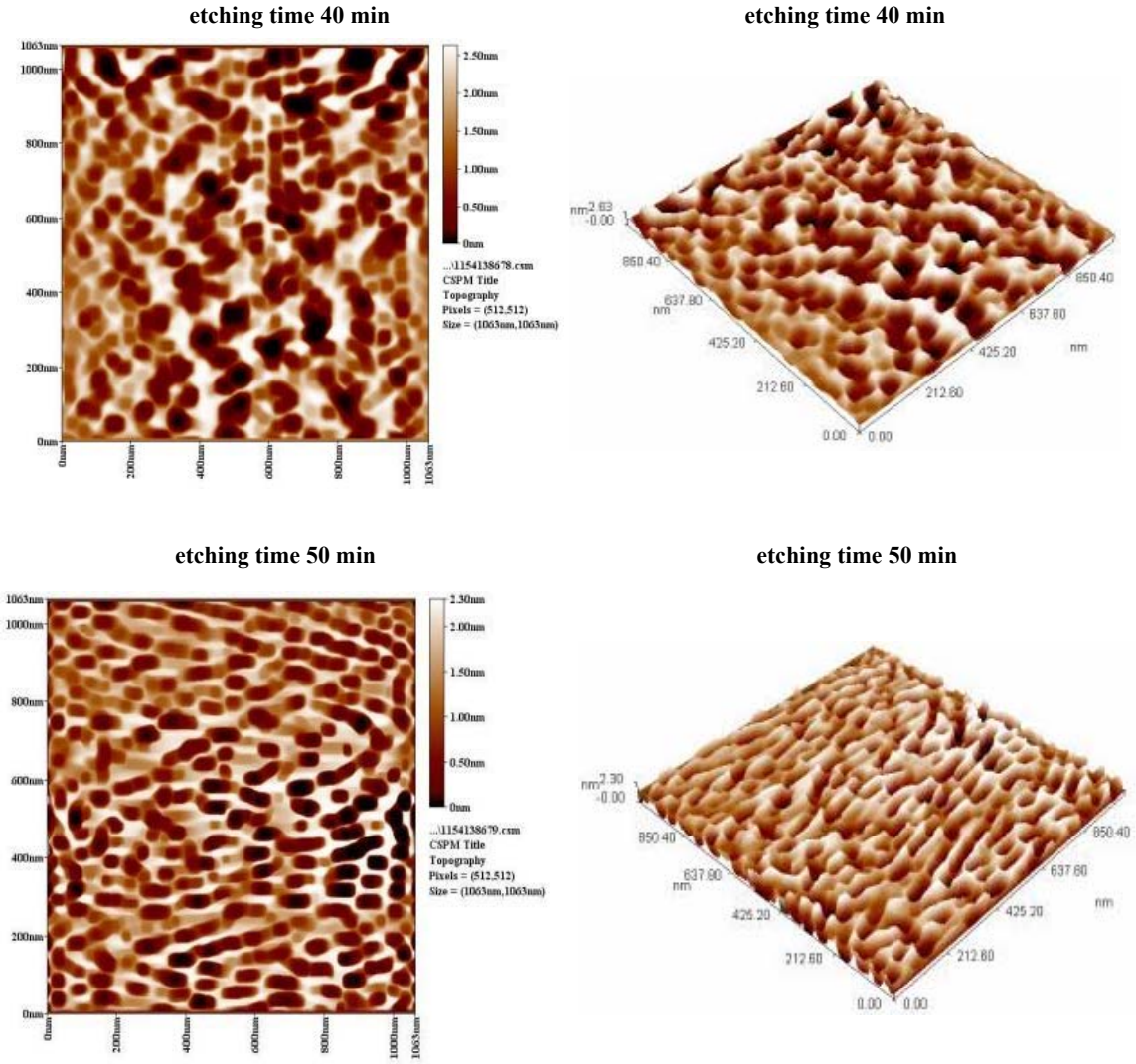


Figure 4. Schematic 2D and 3D image of PS surface at different etching times

Table 2. Parameters for Si and Porous Si wafers at different etching times

| Time (min) | Avg. Diameter (nm) | Avg. Roughness (nm) | Root mean square (nm) |
|---|---|---|---|
| **10** | 80.82 | 0.788 | 0.896 |
| **20** | 57.81 | 0.658 | 0.760 |
| **30** | 53.80 | 0.594 | 0.686 |
| **40** | 40.99 | 0.576 | 0.665 |
| **50** | 35.49 | 0.376 | 0.436 |

The PS layers were formed on the p–type c–Si <111> sample, as shown in Figure 4. The samples exhibited surface roughness and pyramid–like hillocks surfaces. Results show that several pores had sphere–like appearance and sponge–like shape in samples with rough and pyramid–like hillocks surfaces. The estimated average diameter of the pores between 35.49–80.82 nm, whereas the average roughness was between 0.376–0.788 nm. Surface roughness with a depth between 0.58–3.82 nm and 0.45–2.9 nm for PS samples at 10 and 20 min, respectively, validated pore formation. Similarly, for sample PS at 30 min, the depth was about 0–2.83 nm. The PS sample at 40 min had a surface roughness of about 0–50.52 nm, whereas the PS sample at 50 min had a roughness between 0–30.32 nm. These results clearly indicate that an increase in anodization time resulted in an increase in the roughness of the pores. pours structure is due to the charge carrier generation at semiconductor electrolyte

interface by external biasing . When etching time increases, more and more number of carrier which take part in etching process com into the semiconductor electrolyte interface, leading to increase in the pore size, the increase in pore size leads to decrease in sizes of pore wall (Hasan, 2012).

*3.3 Structural Properties*

Figure (5) shows the x–ray diffraction of silicon bulk and PS prepared different etching time at 10, 20, 30, 40, and 50 min. XRD analysis indicated variations between bulk silicon surface and PS surfaces. The x–ray beam was diffracted at specific angular positions with respect to the incident beam depending on the phases of the sample. When the crystal size was reduced to a nanometric scale, a broadening of diffraction peaks was observed and the width of the peak was directly correlated to the size of the nanocrystalline domains (Hasan, 2012). Figure 5 shows that the silicon bulk has a strong peak at $2\theta = 28.38°$ oriented only along the (111) direction. This observation confirms that the monocrystalline structure of the Si layer belongs to the (111) reflecting plane of the cubic structure Si. Crystallite size can be estimated using diffraction pattern analysis, which measures the full width at half maximum (FWHM) measurement and applies the Scherrer equation. The average crystallite size $L$ is

$$L = \frac{k\lambda}{\beta \cos\theta}$$

where λ is the X–ray wavelength in (nm), β is the peak width of the diffraction peak profile at half maximum height resulting from small crystallite size in radians, and K is a constant related to crystallite shape that is normally calibrated as 0.9. K can also be calibrated as 0.89 or 0.9 for FWHM of spherical crystals with cubic unit cells (Lorusso et al., 2009).

The crystallite sizes obtained from crystalline and porous silicon samples are shown in Table 3. Using the Scherrer equation, the value difference of FWHM between Si bulk and PS under various etching times was about 0.1520–0.2770 Deg. The grain size of PS differed at various etching times between 29.6–50.6 nm. A significant decrease in crystallite size was noticed as etching time increased. In the case of porous samples, nanometric dimensions were achieved within a considerably shorter time.

Table 3. Structural parameters: 2θ, $d_{hkl}$, (hkl), FWHM, and G.S of Si wafer at different etching times

| *Etching time* | *2θ (Deg.)* | *FWHM (Deg.)* | *$d_{hkl}$ Exp.(Å)* | *G.S (nm)* | *$d_{hkl}$ Std.* | *hkl* |
|---|---|---|---|---|---|---|
| **Before etching** | 28.3920 | 0.1520 | 3.1410 | 53.9 | 3.1354 | (111) |
| **10** | 28.3810 | 0.1620 | 3.1422 | 50.6 | 3.1354 | (111) |
| **20** | 28.3810 | 0.1740 | 3.1422 | 47.1 | 3.1354 | (111) |
| **30** | 28.3790 | 0.1970 | 3.1424 | 41.6 | 3.1354 | (111) |
| **40** | 28.3590 | 0.2270 | 3.1446 | 36.1 | 3.1354 | (111) |
| **50** | 28.3480 | 0.2770 | 3.1458 | 29.6 | 3.1354 | (111) |

*3.4 Gas Sensor*

The interaction between PS and oxygen is significant for the development of a sensor device because it normally has to work with oxygen present in the air to detect any other gas. This feature indicates that our sensor can be easily applied to air without any influence of oxygen in the environment (Gabouze et al., 2006). The sensors showed excellent performance in terms of response, time of response, time of recovery, and stability. Hence, the PS can be used as a gas sensor depending on factors, such as temperature, grain size, and porosity (Dian, Konečný, Broncová, Kronďák, & Matolínová, 2013). The conductivity of PS layers increased for $NO_2$ gas. Measurements indicate that the $NO_2$ molecules acted as acceptor centers (Pancheri, Oton, Gaburro, Soncini, & Pavesi, 2003).

Free carrier (hole) concentration in the PS layers increased, thereby increasing conductivity. $O_2$ molecules were absorbed into PS layers either by physisorption or weak chemisorption processes. Thus, PL quenching can be attributed to the transient nonradiative electron transfer from the luminescent chromophore in the PS by oxygen (Choi et al., 2009). Electric signals obtained using different fabricated PS samples can produce total specificity for a given gas.

The PS was initially tested to confirm its semiconducting behavior .The sensor was placed on a heater base and its resistance measured as temperature increased from room temperature to 300 °C in dry air atmosphere.

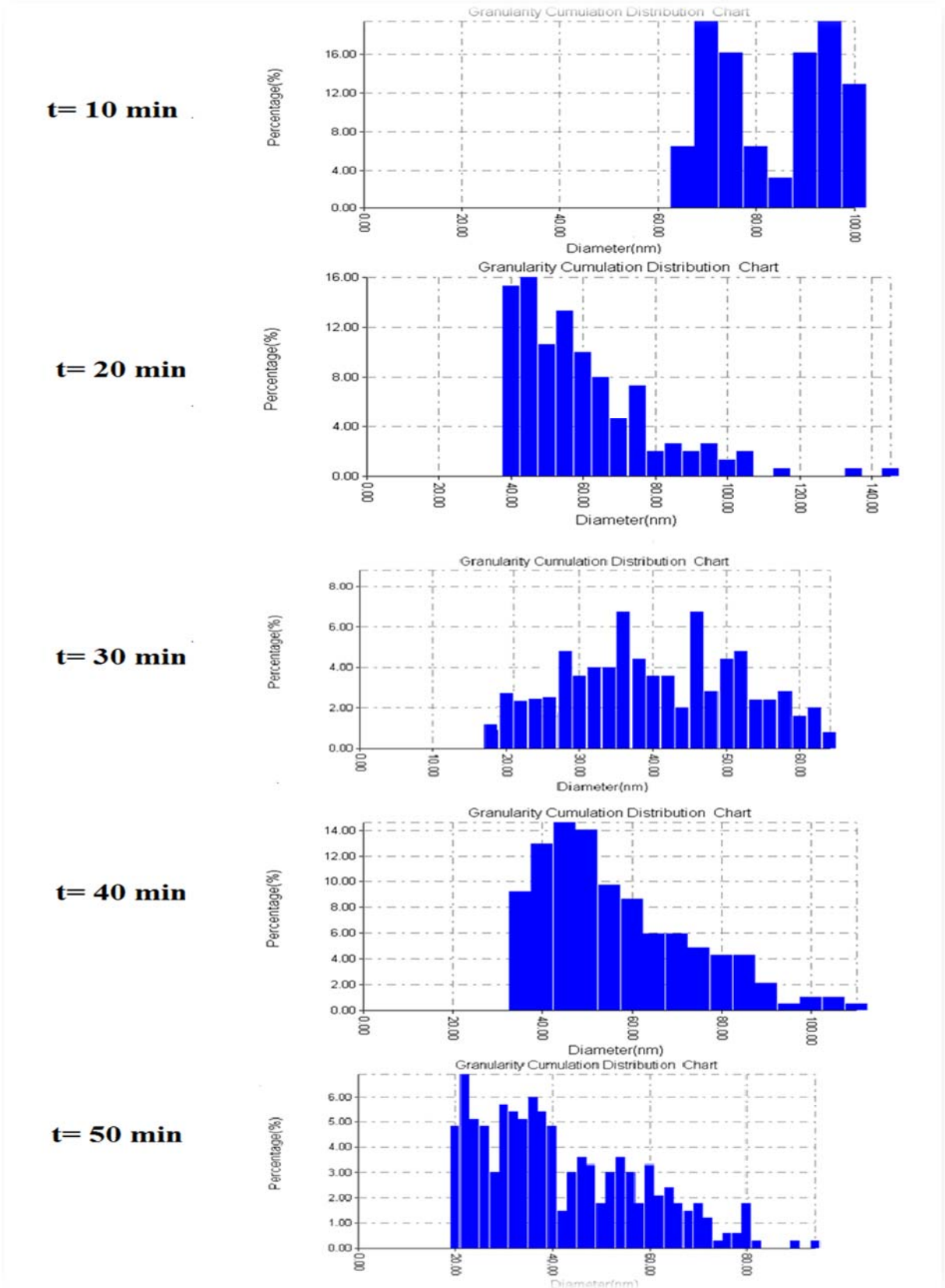


Figure 5. Schematic Granularity Cumulation Distribution Chart for PS at different etching times

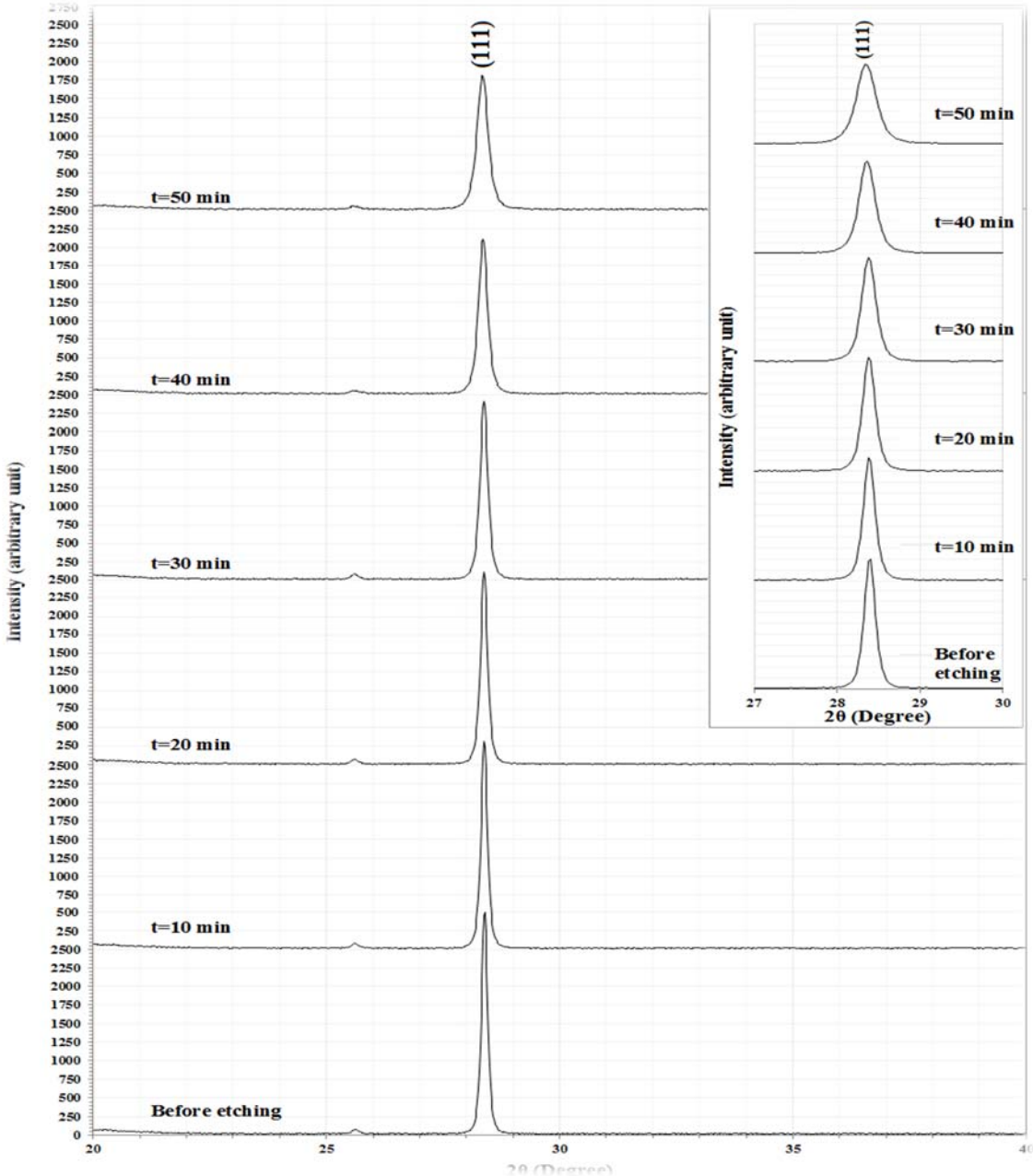


Figure 6. Schematic X–ray diffraction patterns of bulk Si wafer and PS at different etching times

Figure 7 shows the variations in PS sensitivity as a function operation temperature in the range of RT to 300 °C of the PS. The sensing test was performed using 3% $NO_2$. Air mixed ratio and bias voltage (3V) were applied on the electrodes of all samples. Temperature variations revealed the resistance of all films, which decreased when the temperature increased from room temperature to 150 °C, indicating a typical negative temperature coefficient of resistance due to thermal excitation of the charge carriers in the semiconductor. Above 150 °C, the sensor films displayed positive temperature coefficient of resistance as temperature increased further, which could be attributed to the saturation of the conduction band with electrons elevating from shallow donor levels caused by oxygen vacancies. At this point, an increase in temperature will lead to a decrease in electron mobility and a subsequent increase in resistance.

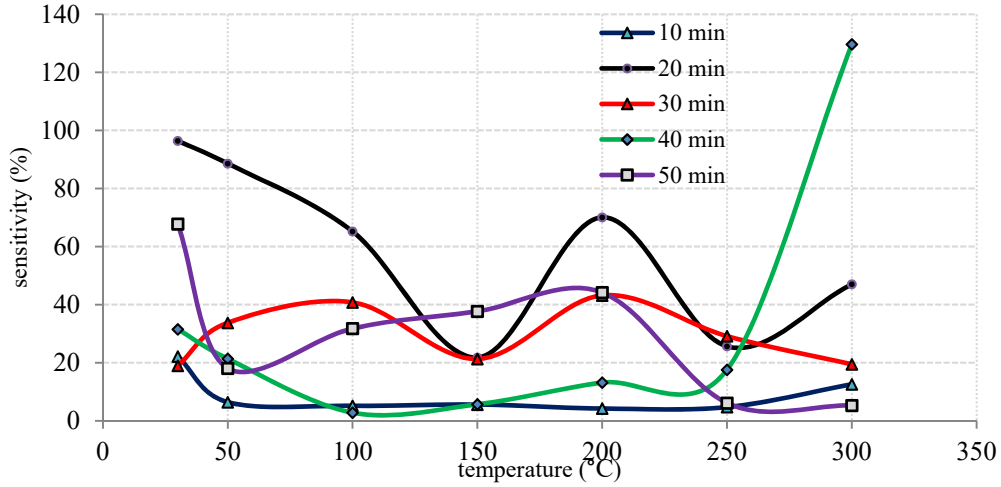


Figure 7. Schematics of the variations of sensitivity with the operating temperatures for different porous times on PS for $NO_2$

The high sensitivity may because of the optimum surface roughness, porosity, large surface area, and large rate of oxidation. The maximum sensitivity of the 20 min PS to $NO_2$ gas is 96.38% at room temperature. Figure (8) shows the variations of sensitivity as a function operation temperature of the PS. The sensing test was performed by oxidizing $NO_2$ gas and reducing $H_2$, gas applied on the best sample at 20 min. The sensing behavior indicated maximum sensitivity for oxidizing $NO_2$ gas in range of room temperature to 150 °C. However, the opposite behavior can be observed for reducing $H_2$ gas. The sensor displays the same behavior for the variations of the temperature of the $NO_2$ and $H_2$ gas above 150 °C or with less selectivity.

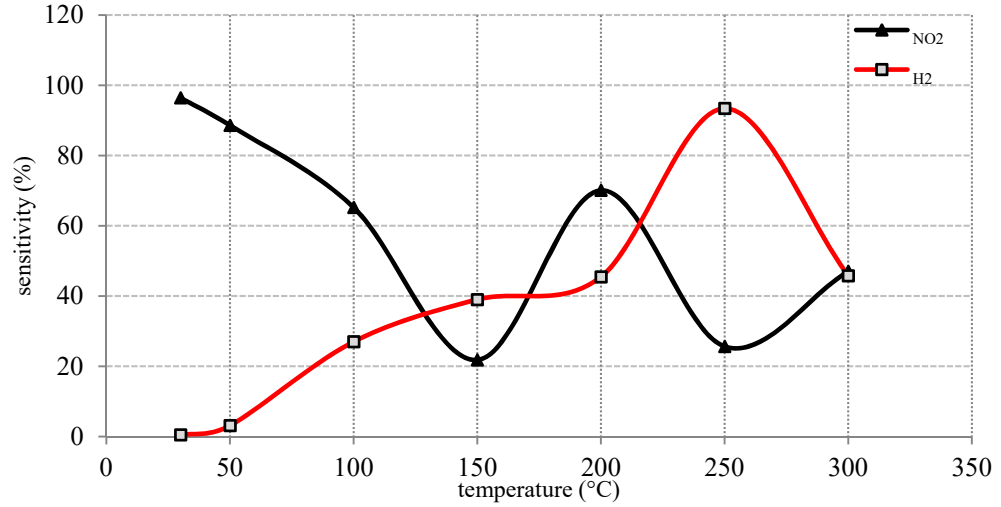


Figure 8. Schematic of the variation sensitivity with operating temperatures for $No_2$ and $H_2$ gas

Figure (9) shows the variations of response time with etching time for different operation temperatures. These figures reveal that response time decreased with increasing etching time at an operation temperature below 200 °C, whereas the response time increased with increasing etching time at higher operation temperature of >200 °C.

The reduction in grain size as the etching time increased allowed the space charge to cover large volumes of the grain and a large number of grain boundaries, thereby providing large areas for $O^-$ and $O^{-2}$ absorption. Large variations in the barrier and resistance can enhance reactivity at lower temperatures. The density of surface states increased with reduction in particle size. Surface states density can also contribute to lowering the operation temperature.

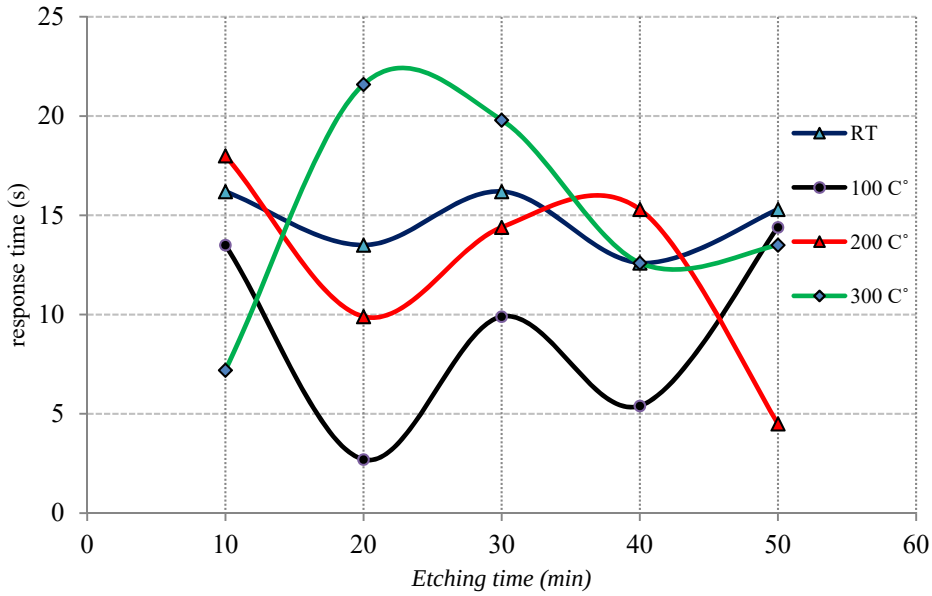


Figure 9. Variations in Response time with porous time for different operating temperatures on PS

## 5. Conclusions

1) PL emissions from nanostructures could be attributed to the nanoscaled size of silicon achieved through quantum confinement effect of the PS. The electronic band gap can be tuned from 1.984–2.455 eV.

2) The AFM analysis showed that the rough silicon surface, which can be viewed as a condensation point for small skeleton clusters, plays an important role in the strength of the visible luminescence and the nanocrystalline PS. The analysis further shows that the rough silicon surface with increasing in etching time orders the small pores to exhibit sponge–like structures, thereby increasing pore diameter.

3) XRD properties indicated the porous monocrystalline structure, the nanoscaled size decrease and the broadening of the PS peaks.

4) The PS structure can be used in $NO_2$ and $H_2$, and gas sensors. The response time of several seconds depends on the porosity of the PS samples.

## References

Agarwal, V., & Del Rıo, J. A. (2003). Tailoring the photonic band gap of a porous silicon dielectric mirror. *Applied physics letters*, *82*(10), 1512-1514.

Bratkowski, A., Korcala, A., Łukasiak, Z., Borowski, P., & Bała, W. (2005). Novel gas sensor based on porous silicon measured by photovoltage, photoluminescence, and admittance spectroscopy. *Opto-electronics review*, *13*(1), 35-38.

Choi, S. H., Cheng, H., Park, S. H., Kim, H. J., Kim, Y. Y., & Lee, K. W. (2009). A study of the gas specificity of porous silicon sensors for organic vapours. *Materials science–Poland*, *27*, 603-610.

Dian, J., Konečný, M., Broncová, G., Kronďák, M., & Matolínová, I. (2013). Electrochemical fabrication and characterization of porous silicon/polypyrrole composites and chemical sensing of organic vapors. *Int. J. Electrochem. Sci*, *8*, 1559-1572.

Doğan, Ş., Akın, N., Başköse, C., Asar, T., Memmedli, T., & Özçelik, S. (2013). Porous Silicon: Volume-Specific Surface Area Determination from AFM Measurement Data. *Journal of Materials Science and Engineering B, 3*(8) 518–523.

Dubey, R. S., & Gautam, D. K. (2009). Synthesis and Characterization of Nanocrystalline Porous Silicon Layer for Solar Cells Applications. *Journal of Optoelectronic and Biomedical Materials, 1*.

Dubey, R. S., Patil, L. S., Bange, J. P., & Gautam, D. K. (2007). Optoelectron and Adv. *Mater.–Rapid Commun*, *1*(12), 655.

Gabouze, N., Belhousse, S., Cheraga, H., Ghellai, N., Ouadah, Y., Belkacem, Y., & Keffous, A. (2006). CO 2 and H 2 detection with a CHx/porous silicon-based sensor. *Vacuum*, *80*(9), 986-989.

Galeazzo, E., Peres, H. E. M., Santos, G., Peixoto, N., & Ramirez-Fernandez, F. J. (2003). Gas sensitive porous silicon devices: responses to organic vapors. *Sensors and Actuators B: Chemical*, *93*(1), 384-390.

Galeazzo, E., Peres, H. E. M., Santos, G., Peixoto, N., & Ramirez-Fernandez, F. J. (2003). Gas sensitive porous silicon devices: responses to organic vapors. *Sensors and Actuators B: Chemical*, *93*(1), 384-390.

Hadi, H. A., Ismail, R. A., & Habubi, N. F. (2013). Fabrication and characterization of porous silicon layer prepared by photo-electrochemical etching in CH3OH: HF solution. *International Letters of Chemistry, Physics and Astronomy*, *3*, 29-36.

Halimaoui, A., Oules, C., Bomchil, G., Bsiesy, A., Gaspard, F., Herino, R., ... & Muller, F. (1991). Electroluminescence in the visible range during anodic oxidation of porous silicon films. *Applied Physics Letters*, *59*(3), 304-306.

Hasan A. H. (2012). *Fabricion and characterization of porous silicon* (Ph.D. thesis). College of Education University of Al Mustansiyriay.

Jalkanen, T., Tuura, J., Mäkilä, E., & Salonen, J. (2010). Electro-optical porous silicon gas sensor with enhanced selectivity. *Sensors and Actuators B: Chemical*, *147*(1), 100-104.

Lee, K. H., Jeon, K. S., Lee, S. K., & Choi, C. S. (2003). Photoluminescence Tuning of Porous Silicon by Electrochemical Etching in Mixed Electrolytes.*Journal of Photoscience*, *10*(3), 257-261.

Lehmann, V., & Gösele, U. (1991). Porous silicon formation: a quantum wire effect. *Applied Physics Letters*, *58*(8), 856-858.

Lorusso, A., Nassisi, V., Congedo, G., Lovergine, N., Velardi, L., & Prete, P. (2009). Pulsed plasma ion source to create Si nanocrystals in SiO 2 substrates. *Applied Surface Science*, *255*(10), 5401-5404.

Marotti, R. E., Quagliata, E., & Dalchiele, E. A. (2003). Photoluminescence from photochemically etched silicon. *Solar energy materials and solar cells*, *76*(3), 263-279.

Mishra, V., Patel, P. N., & Vohra, T. (2014). Realization of Pporous silicon Ns And Sstructures For optical Ddetection on of petrol Aadulteration. *Digest Journal of Nanomaterials and Biostructures, 9*(3), 96 –974,

Mizsei, J. (2007). Gas sensor applications of porous Si layers. *Thin solid films*, *515*(23), 8310-8315.

Mizuno, H., Koyama, H., & Koshida, N. (1996). Oxide‐free blue photoluminescence from photochemically etched porous silicon. *Applied physics letters*, *69*(25), 3779-3781.

Möller, F., Chorin, M. B., & Koch, F. (1995). Post-treatment effects on electrical conduction in porous silicon. *Thin Solid Films*, *255*(1), 16-19.

Monshi, A., Foroughi, M. R., & Monshi, M. R. (2012). Modified Scherrer equation to estimate more accurately nano-crystallite size using XRD. *World Journal of Nano Science and Engineering*, *2*(03), 154.

Nayef, U. (2013). Fabrication and Characteristics of Porous Silicon for Photoconversion. *International Journal of Basic & Applied Sciences IJBAS-IJENS*, *13*(2), 61.

Nayef, U. M.., & Muayad, M. W. (2013) Typical of Morphological Properties of Porous Silicon. *International Journal of Basic & Applied Sciences IJBAS–IJENS, 13*(2).

Oton, C. J., Dal Negro, L., Gaburro, Z., Pavesi, L., Johnson, P. J., Lagendijk, A., & Wiersma, D. S. (2003). Light propagation in one‐dimensional porous silicon complex systems. *Physica status solidi (a)*, *197*(1), 298-302.

Pancheri, L., Oton, C. J., Gaburro, Z., Soncini, G., & Pavesi, L. (2003). Very sensitive porous silicon NO 2 sensor. *Sensors and Actuators B: Chemical*, *89*(3), 237-239.

Parkhutik, V. (1999). Porous silicon mechanical of growth and application. *Solid State Electronic, 43*, 1121–1141.

Rothschild, A., & Komem, Y. (2004). The effect of grain size on the sensitivity of nanocrystalline metal-oxide gas sensors. *Journal of Applied Physics*, *95*(11), 6374-6380.

Salcedo, W. J., Ramirez Fernandez, F. J., & Galeazzo, E. (1997). Structural characterization of photoluminescent porous silicon with FTIR spectroscopy.*Brazilian Journal of Physics*, *27*, 158-161.

Šalucha, K., & Marcinkevičius, A. J. (2007). Investigation of Porous Silicon Layers as Passivation Coatings for High Voltage Silicon Device. *Electronics and Electrical Engineering*, (79) 41–44.

Saplagio, N. G. E., Mabilangan, A. I., Faustino, M. A. B., Lopez Jr, L. P., Somintac, A. S., & Salvador, A. A. (2014). Tunable Photonic Crystals Based on Electrochemically Etched Porous Silicon. *Int. J. Electrochem. Sci*, *9*, 6191-6200.

Setzu, S., Ferrand, P., & Romestain, R. (2000). Optical properties of multilayered porous silicon. *Materials Science and Engineering: B*, *69*, 34-42.

Skryshevsky, V. A. (2000). Photoluminescence of inhomogeneous porous silicon at gas adsorption. *Applied surface science*, *157*(3), 145-150.

Smith, R. L., & Collins, S. D. (1992). Porous silicon formation mechanisms.*Journal of Applied Physics*, *71*(8), R1-R22.

Timokhov, D. F., & Timokhov, F. P. (2004). Denervation of structure parameters of porous silicon by the photoelectric method. *Journal of physical studies, 8*(2), 173-177.

Watanabe, K., Okada, T., Choe, I., & Sato, Y. (1996). Organic vapor sensitivity in a porous silicon device. *Sensors and Actuators B: Chemical, 33*(1), 194-197.